Dynamic subgrid-scale scalar-flux model based on the exact rate of production of turbulent fluxes

Shujaut H. Bader* and Paul A. Durbin†
Department of Aerospace Engineering, Iowa State University, Ames, Iowa 50011, USA

(Received 19 April 2020; accepted 27 October 2020; published 19 November 2020)

A dynamic subgrid-scale (SGS) scalar-flux model, based on the exact rate of production of turbulent scalar fluxes, is proposed. The model is derived from an assumption that the pressure-scalar correlation in the equation for turbulent scalar flux is a vector that is approximately aligned with the scalar flux itself. The formulation then yields a tensor diffusivity which allows nonalignment of the SGS scalar fluxes with respect to the resolved scalar gradient. In contrast to eddy diffusivity models and to general gradient diffusion hypothesis models, for which the diffusivity tensor is symmetric, the present formulation produces an asymmetric diffusion tensor; for theoretical and experimental reasons, that tensor is known to be very asymmetric. The model contains a single coefficient, which is determined dynamically. The model is validated in fully developed turbulent channel flow and in separated and reattaching flow over a backstep.

DOI: 10.1103/PhysRevFluids.5.114609

I. INTRODUCTION

Passive scalar transport is important in many flows of practical interest: the rate of mixing in reacting flows, transport of contaminants, and dispersion of internal energy driven by small temperature variations are some examples where modeling the passive scalar fields plays an important role.

Advances in scientific computing have made large eddy simulation (LES) a preferred approach to simulate the underlying physics of hydrodynamic and scalar fields, at a relatively lower cost than direct numerical simulations (DNS). To effect that efficiency, LES requires closure formulations to replace unresolved quantities, that arise from filtering the governing equations. It is imperative to model these unresolved quantities, as they are representative of turbulent dispersion at scales smaller than the filter width. In a sense, the predictive power of an LES depends to a significant extent upon how effective the subgrid model is in parameterize the physics of small scales.

Closures for the subgrid scale (SGS) scalar flux follow those that have been devised for Reynolds averaged modeling, the simplest being a simple gradient diffusion hypothesis (SGDH). This invokes a scalar subgrid diffusivity, often equated to the subgrid viscosity divided by a turbulent Prandtl number. The dynamic procedure of Germano [1] was employed by Moin *et al.* [2] to evaluate the subgrid diffusivity directly, which provides the dynamic eddy diffusivity model (Dyn-EDM). A method to determine the subgrid Prandtl number dynamically, without invoking the Germano identity, was developed by Yin and Durbin [3], and found to be more accurate than Dyn-EDM.

*shbader@iastate.edu
†durbin@iastate.edu

By invoking an isotropic turbulent diffusivity, the SGDH assumes alignment of the instantaneous SGS scalar flux and resolved scalar gradient,

$$h_{i\theta}^{\mathrm{EDM}} = -\alpha_T \, \partial\overline{\theta}/\partial x_i,$$

and thus fails to represent the anisotropic effects encountered in complex 3D flows. That error may have a small influence on the predictions of the average scalar concentration profile, because only the wall normal flux contributes to the mean flux divergence [4], but the fluctuating fluxes will be inaccurate. Thus there is cause to consider a more physically justified subgrid closure.

It has been noted in several studies [5] that the turbulent diffusivity is not independent of orientation of the mean scalar gradient. Numerical investigations of homogenously sheared turbulence [6] have revealed that the turbulent Prandtl number is significantly smaller than 0.9 [7] when the applied mean scalar gradient is orthogonal to the mean shear. Thus, in such situations, the scalar turbulent diffusivity is grossly in error, thereby questioning the physical relevance of scalar turbulent diffusivity models. Such considerations argue for the turbulent diffusivity to be represented by a tensor, i.e.,

$$h_{i\theta} = -\alpha_{T_{ij}} \partial\overline{\theta}/\partial x_j,$$

where $\alpha_{T_{ij}}$ is asymmetric [4]. Models with tensor diffusivity rotate the SGS flux vector with respect to the resolved scalar gradient, and yield scalar fluxes in directions other than that of the imposed mean scalar gradient—hence the name generalized gradient diffusion hypothesis (GGDH). Daly and Harlow [8] suggested a constitutive relation

$$h_{i\theta}^{\mathrm{GGDH}} = -C_{G\theta} \mathscr{T} \tau_{ij} \frac{\partial\overline{\theta}}{\partial x_j}$$

based on the Reynolds stress tensor, τ_{ij}. Wang *et al.* [9], and Peng and Davidson [10] extended it to LES for active and passive scalars by using the deviatoric part of the SGS stress tensor in place of τ_{ij}, and adopted the dynamic method [1] to compute the model coefficient locally. This will be referred to as Dyn-GGDH hereinafter.

Wang *et al.* [9] extended the original GGDH approach to incorporate a full linear as well as a quadratic tensor diffusivity, derived according to the theory of tensor polynomial functions. Invoking tensor representations, Wang *et al.* [11] have also expressed the SGS scalar-flux vector as a function of resolved strain rate and rotation rate tensors and the resolved scalar gradient. Note, however, that these models with higher order nonlinear tensor diffusivity are not derived from the transport equation of the SGS scalar fluxes. Moreover, computing the additional terms arising in the zeroth-order, linear, and quadratic tensorial polynomial components requires additional numerical operations and adds expense and stiffness. In addition to the various functional forms, many structural modeling recipes have been prescribed for the SGS scalar fluxes. One example would be the extension of scale similarity models for SGS stresses [12] to SGS scalar fluxes. As a consequence of relating the SGS closure directly to the smallest resolved scales, these models are generally better at predicting the structure of the SGS fluxes, but deal inadequately with the transfer of scalar energy between the resolved and the subgrid scales. To remedy their underdissipative character, scale-similar models must be supplemented with a dissipative term [13], resulting in a mixed model. Salvetti and Banerjee [14] proposed a dynamic mixed model for the SGS scalar-flux vector, in which the scale similarity term is added to the simple eddy diffusivity model. To avoid the problems associated with functional models, some studies [15] have also proposed regularization of the gradient model to avoid the backscatter of scalar variance. Their idea is to neglect the stretching effect in the model formulation by considering the part of the filtered strain rate tensor built only with the negative eigenvalues. Other approaches include modulated gradient model [16], which computes the structure of the subgrid flux based on the normalized gradient vector, derived from the Taylor expansion of the exact subgrid flux. The magnitude of the flux is computed from the relevant subgrid scales which are estimated based on the local-equilibrium hypothesis.

In light of these considerations, we propose herein a dynamic SGS scalar-flux model based on the exact rate of production of turbulent fluxes and a semiequilibrium scalar-flux assumption. The semiequilibrium approximation consists of ignoring the transport and nonhomogeneous terms. It is not a consistent equilibrium approximation, because the fluxes are not scaled [17]; rather it is seen as a route to devise an algebraic model. In this work, we advance this idea, taken from the RANS literature, to the framework of SGS modeling. The focus of the present work is on the development of a robust and inexpensive tensor diffusivity SGS scalar-flux model, having an explicit dependence on the SGS stress tensor and on the resolved shear rate. The shear is the cause of $\alpha_{T_{ij}}$ being asymmetric.

II. MATHEMATICAL FORMULATION

A. Governing equations

The filtered, LES, continuity, momentum, and passive scalar transport equations are

$$\frac{\partial \overline{u}_i}{\partial x_i} = 0, \quad \frac{\partial \overline{u}_i}{\partial t} + \overline{u}_j \frac{\partial \overline{u}_i}{\partial x_j} = -\frac{1}{\rho}\frac{\partial \overline{p}}{\partial x_i} + \nu \frac{\partial^2 \overline{u}_i}{\partial x_j \partial x_j} - \frac{\partial \tau_{ij}}{\partial x_j},$$
$$\frac{\partial \overline{\theta}}{\partial t} + \frac{\partial}{\partial x_j}(\overline{u}_j \overline{\theta}) = \alpha \frac{\partial^2 \overline{\theta}}{\partial x_j \partial x_j} - \frac{\partial h_{j\theta}}{\partial x_j}, \tag{1}$$

where $\overline{\theta}$ is the filtered passive scalar, α is the molecular diffusion coefficient, $h_{j\theta}$ is the SGS scalar-flux vector which needs to be parameterized, and the remaining symbols have their usual meanings. In the following subsection, the derivation and the implementation of the proposed SGS scalar-flux model are described.

B. SGS scalar-flux model

1. Model derivation

The most general expression for the transport equation of the SGS scalar flux, $h_{i\theta} = \overline{u_i\theta} - \overline{u}_i\overline{\theta}$, is [13]

$$\frac{D}{Dt} h_{i\theta} = \mathcal{P}^{\mathrm{SGS}}_{i\theta} - \mathcal{E}^{\mathrm{SGS}}_{i\theta} + \Pi^{\mathrm{SGS}}_{i\theta} + \mathcal{D}^{\mathrm{SGS}}_{i\theta}, \tag{2}$$

where

$$\mathcal{P}^{\mathrm{SGS}}_{i\theta} = -\tau_{ij}\frac{\partial \overline{\theta}}{\partial x_j} - h_{j\theta}\frac{\partial \overline{u}_i}{\partial x_j}, \quad \mathcal{E}^{\mathrm{SGS}}_{i\theta} = (\alpha + \nu)\left\langle \frac{\partial \theta}{\partial x_j}, \quad \frac{\partial u_i}{\partial x_j} \right\rangle,$$
$$\Pi^{\mathrm{SGS}}_{i\theta} = \frac{1}{\rho}\left\langle p, \frac{\partial \theta}{\partial x_i} \right\rangle, \quad \mathcal{D}^{\mathrm{SGS}}_{i\theta} = -\frac{\partial}{\partial x_j}\left(\langle u_i, u_j, \theta \rangle + \frac{\delta_{ij}}{\rho}\langle p, \theta \rangle - \alpha \left\langle u_i, \quad \frac{\partial \theta}{\partial x_j} \right\rangle - \nu \left\langle \theta, \quad \frac{\partial u_i}{\partial x_j} \right\rangle \right).$$

The terms on the right of Eq. (2) represent production, dissipation, pressure-scalar correlation, and molecular and turbulent diffusion, respectively. The angled bracket operation represents the Germano notation [1] for a typical LES filter.

Assuming local equilibrium, we conveniently drop the transport and nonhomogeneous terms and invoke the small-scale isotropy assumption, that $\mathcal{E}_{i\theta} \approx 0$. This leaves the pressure-scalar correlation to be modeled. For homogeneous shear and Reynolds averaged equations, Rogers *et al.* [6] have shown that both the pressure-scalar correlation term and the time change of scalar flux are approximately aligned with the scalar flux itself. Hence, for filtered fields, we adopt a simple, relaxation model,

$$\Pi^{\mathrm{SGS}}_{i\theta} = -\frac{h_{i\theta}}{C_\theta \mathscr{T}},$$

where $\mathscr{T}$ is a timescale for relaxation and C_θ a dimensionless constant.

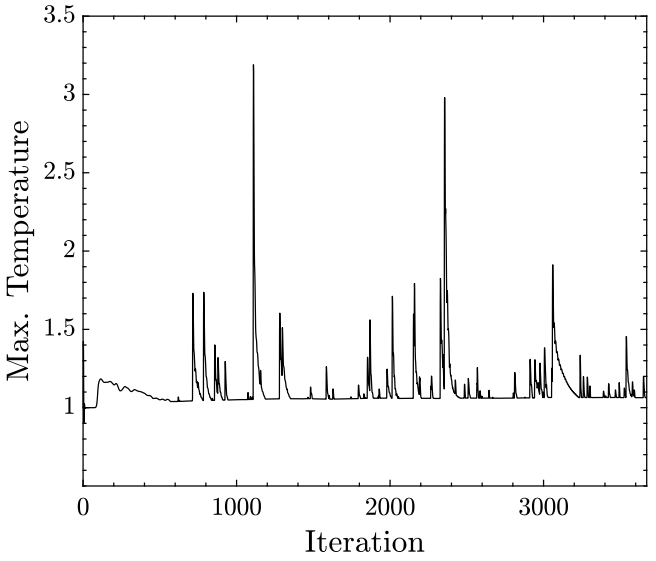

FIG. 1. Rapid variation in the scalar field calculated by Eq. (6) in plane channel flow.

Along with these assumptions, keeping the production term and the time derivative, Eq. (2) becomes

$$\frac{\partial h_{i\theta}}{\partial t} = -\tau_{ij}\frac{\partial \overline{\theta}}{\partial x_j} - h_{j\theta}\frac{\partial \overline{u}_i}{\partial x_j} - \frac{1}{C_\theta \mathscr{T}} h_{i\theta}. \tag{3}$$

As the resulting system is implicit in scalar fluxes, for ease of numerical implementation, at any time level, n, we follow RANS numerics [4] by treating the second and third term on the right-hand side (RHS) of Eq. (3) explicitly and implicitly, respectively,

$$\frac{h^n_{i\theta} - h^{n-1}_{i\theta}}{\Delta t} = -\tau_{ij}\frac{\partial \overline{\theta}}{\partial x_j} - h^{n-1}_{j\theta}\frac{\partial \overline{u}_i}{\partial x_j} - \frac{1}{C_\theta \mathscr{T}} h^n_{i\theta}. \tag{4}$$

This was tested as a method to update the SGS scalar flux at each time step. The results differed little from the simplified version that we finally adopted. The SGS scalar fluxes are dominated by length scales of the order of the filter width [18], and the corresponding time scales are 5–10 times larger than the time step [19]. Based on these observations, the model is simplified by dropping the time derivative and, finally, written as

$$h^n_{i\theta} = -C_\theta \mathscr{T}\left(\tau_{ij}\frac{\partial \overline{\theta}}{\partial x_j} + h^{n-1}_{j\theta}\frac{\partial \overline{u}_i}{\partial x_j}\right). \tag{5}$$

For RANS, Rogers *et al.* [6] solved the steady state version of Eq. (3) via a matrix inversion, $\mathscr{O}^{-1} = (I + C_\theta \mathscr{T} \nabla \overline{\mathbf{u}})^{-1}$,

$$h_{i\theta} = -C_\theta \mathscr{T} \mathscr{O}^{-1}_{in} \tau_{nj} \frac{\partial \overline{\theta}}{\partial x_j}. \tag{6}$$

However, as those authors report, this approach has been observed to produce a stiff matrix $\mathscr{O}_{ij}$ for some values of the model coefficient C_θ, leading to a rapid variation in the solution as shown in Fig. 1. Younis *et al.* [20] pointed out a more serious problem of Eq. (6) becoming singular in the case of plane strain. Singular, or near singular, behavior indicates that the equilibrium approximation is not valid.

It is to circumvent these numerical issues and to extend the applicability of the model to SGS modeling that we have proposed a simple explicit approach, as described above in Eq. (5). Using the basic representation of a tensor diffusivity,

$$h_{i\theta} = -\alpha_{T_{ij}} \frac{\partial \overline{\theta}}{\partial x_j}, \tag{7}$$

in Eq. (5), that equation can be expressed as

$$\alpha^n_{T_{ij}} = C_\theta \mathscr{T} \left(\tau_{ij} - \alpha^*_{T_{kj}} \frac{\partial \overline{u}_i}{\partial x_k} \right), \tag{8}$$

with $\alpha^*_{T_{kj}} = \alpha^{n-1}_{T_{kj}}$. The scalar gradient has been evaluated at time n and removed. This equation depends only on properties of the turbulence, and not on the scalar field, as a turbulent diffusion coefficient should. The subgrid stress tensor is given by

$$\tau_{ij} = \tfrac{2}{3}\delta_{ij} k_{\rm sgs} - 2\nu_{\rm sgs}\overline{S}_{ij},$$

with the Smagorinsky eddy viscosity and with (A3) for the isotropic stress $k_{\rm sgs}$. Equations (7) and (8) are the basis of the SGS scalar-flux model. The switch from (5) to the gradient diffusion form (7) allows the flux to be implemented numerically as an implicit diffusion term, in the temperature equation. Also, a more formal equilibrium assumption [17] requires that approximation to be applied to a diffusion tensor, independent of the scalar gradient.

Equation (8) together with (7) represent the model forms. The results obtained by this approximation are reasonably accurate, reduce the number of operations, and increase the robustness. No attempt was made to use a higher-order approximation for $\alpha_{T_{ij}}$. This approximation also makes the dynamic evaluation of C_θ straightforward.

2. *Model implementation*

To close Eq. (8), the coefficient $C_\theta(\mathbf{x}, t)$ is computed by minimizing the error norm of the Germano identity as follows. At grid-filter level, $\overline{(\,)}$, the SGS scalar-flux vector is

$$h_{i\theta} = -C_\theta \overline{\mathscr{T}} \left(\tau_{ij} - \overline{\alpha}^*_{T_{kj}} \frac{\partial \overline{u}_i}{\partial x_k} \right) \frac{\partial \overline{\theta}}{\partial x_j}. \tag{9}$$

At test-filter level, $\widehat{(\,)}$, the SGS scalar-flux vector is

$$H_{i\theta} = -C_\theta \widehat{\overline{\mathscr{T}}} \left(T_{ij} - \widehat{\overline{\alpha}}^*_{T_{kj}} \frac{\partial \widehat{\overline{u}}_i}{\partial x_k} \right) \frac{\partial \widehat{\overline{\theta}}}{\partial x_j}, \tag{10}$$

where τ_{ij} and T_{ij} represent the full SGS stress tensors at grid and test filter levels, respectively. The deviatoric parts of τ_{ij} and T_{ij} are evaluated using the dynamic Smagorinsky model [21], while the isotropic parts are computed by invoking the assumption of a local balance between the SGS energy production and dissipation; see (A3) in the Appendix.

The characteristic timescale at both filter levels is evaluated by using the norm of the resolved strain rate tensor, $\mathscr{T} = 1/|\overline{S}|$. Since $|\overline{S}|$ is a feature of length scales of the order of the filter width, and as the SGS scalar flux is dominated by those scales, the timescale derived from it gives a consistent magnitude of the flux [18].

We define vectors $N_{i\theta}$ and $M_{i\theta}$ at grid-filter and test-filter levels, respectively,

$$N_{i\theta} = \frac{1}{|\overline{S}|} \left(\tau_{ij} - \overline{\alpha}^*_{T_{kj}} \frac{\partial \overline{u}_i}{\partial x_k} \right) \frac{\partial \overline{\theta}}{\partial x_j}, \quad M_{i\theta} = \frac{1}{\widehat{|\overline{S}|}} \left(T_{ij} - \widehat{\overline{\alpha}}^*_{T_{kj}} \frac{\partial \widehat{\overline{u}}_i}{\partial x_k} \right) \frac{\partial \widehat{\overline{\theta}}}{\partial x_j}. \tag{11}$$

With these, Eqs. (9) and (10) become

$$h_{i\theta} = -C_\theta N_{i\theta}, \quad H_{i\theta} = -C_\theta M_{i\theta}. \tag{12}$$

We invoke the Germano identity for scalar fluxes,

$$F_{i\theta} = H_{i\theta} - \widehat{h}_{i\theta}, \tag{13}$$

where

$$F_{i\theta} \equiv \widehat{\overline{u}_i\overline{\theta}} - \widehat{\overline{u}}_i\widehat{\overline{\theta}}$$

is a scalar flux, directly computable from the resolved turbulence, and substitute the model (12) into Eq. (13),

$$F_{i\theta} = -C_\theta(M_{i\theta} - \widehat{N}_{i\theta}) = -C_\theta G_{i\theta}, \tag{14}$$

where $G_{i\theta} = (M_{i\theta} - \widehat{N}_{i\theta})$ is a differential vector. Equation (14) is regarded as a method to prescribe C_θ. As this is overdetermined, the solution will be prescribed as the least-squares minimization. In the interest of robustness, the minimization is carried out after summing over all cell faces, treating C_θ as a constant:

$$\min \sum_{\text{faces}} (F_{i\theta} + C_\theta G_{i\theta})^2.$$

Then

$$C_\theta = -\frac{\langle G_{i\theta} F_{i\theta}\rangle}{\langle G_{i\theta} G_{i\theta}\rangle}, \tag{15}$$

where $\langle \cdot \rangle$ denotes the local average of the quantity over the cell faces. This value of C_θ is used on the right side of (8) to update $\alpha_{T_{ij}}$.

In the following sections predictions are compared to the Dyn-EDM and Dyn-GGDH models. For reference, the model forms of Dyn-EDM and Dyn-GGDH are

$$\text{Dyn-EDM:} \quad h_{i\theta}^{\text{EDM}} = -C_{E\theta}\overline{\Delta}^2|\overline{S}|\frac{\partial\overline{\theta}}{\partial x_i}, \tag{16}$$

$$\text{Dyn-GGDH:} \quad h_{i\theta}^{\text{GGDH}} = -C_{G\theta}\frac{\tau_{ij}}{|\overline{S}|}\frac{\partial\overline{\theta}}{\partial x_j}, \tag{17}$$

where $C_{E\theta}$ and $C_{G\theta}$ are dynamically computed model coefficients and the remaining symbols have their usual meanings.

The variation of model coefficients across a turbulent channel flow, for all the three models, is shown in Fig. 2. From Figs. 2(a) and 2(b), it is observed that the model coefficient of the proposed model is much different from the other two. The coefficient of the proposed model is larger than those of Dyn-EDM and Dyn-GGDH, throughout the channel. In the core of the channel, away from the walls, the coefficient of all models remains approximately constant. Figure 3 compares C_θ at $\text{Re}_\tau = 395,\ 640$, and 1020. Inner and outer regions are seen at all Reynolds numbers.

The ratio of the Smagorinksy coefficient for the Dyn-EDM, to the SGS flux model coefficient, gives the turbulent Prandtl number Pr_T. No such interpretation of this ratio exists for models with tensor diffusivities. In our simulations, the negative values of the model coefficients were not clipped; hence, in Fig. 2(c), the instantaneous values of the model coefficient of some of the models may be negative. In the case of the proposed model, negative values are sometimes observed very near the wall, but not in the case shown in the plots. Contours of model coefficients at $y^+ = 5$ are provided in Fig. 4. They are elongated in the direction of shear, as expected. $C_{G\theta}$ and $C_{E\theta}$ show negative patches, while C_θ is entirely positive.

In the EDM model, for the SGS heat flux to go to zero at the walls, the model coefficient must go to zero. However, this is not a requirement for the present model. Since the SGS stress tensor is the nonhomogeneous term in Eq. (8), the modeled SGS heat flux tends to zero by virtue of the stress tensor going to zero. To construct the eddy diffusivity tensor, we have used the full SGS stress

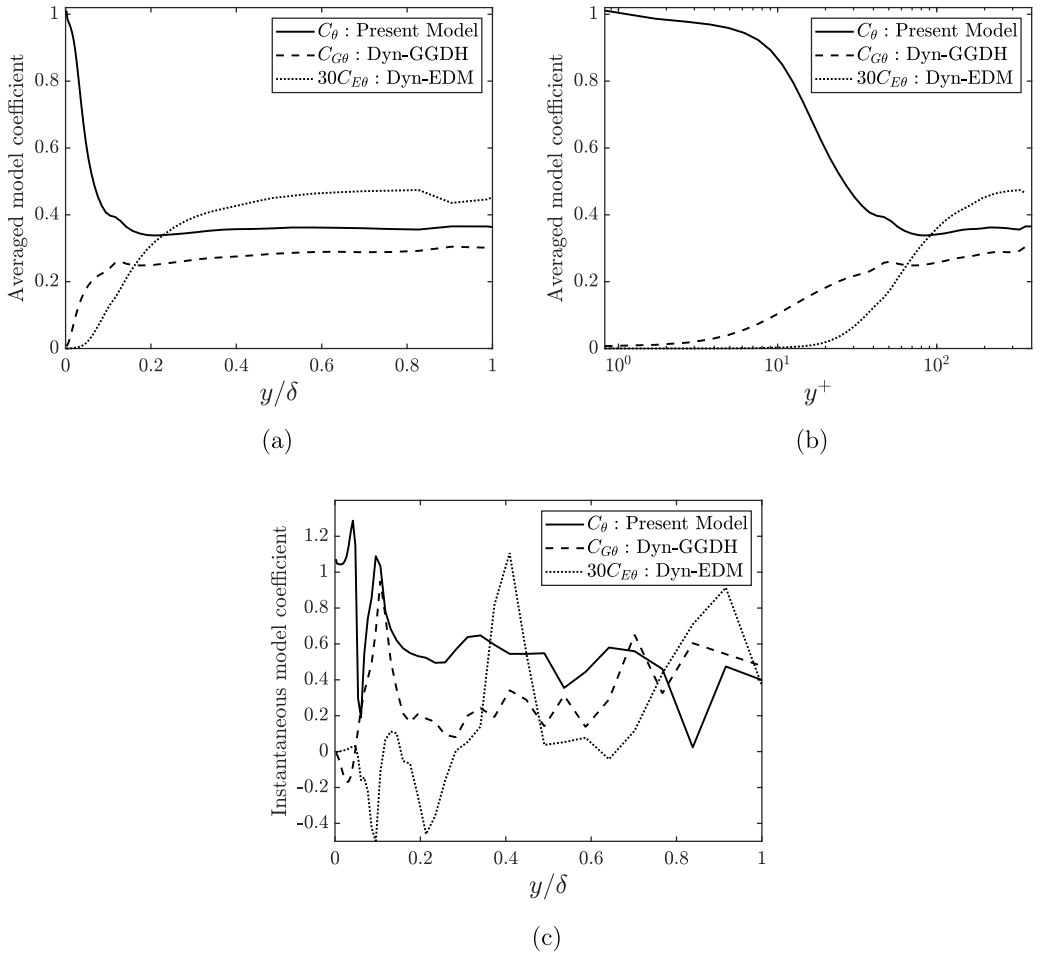

FIG. 2. Averaged model coefficients in fully developed turbulent channel flow at $\mathrm{Re}_\tau = 395$ for different models: in outer scaling (a), in inner scaling (b), and their instantaneous values at $x/L_x = z/L_z = 0.5$ in outer scaling (c).

tensor consisting of the dynamic Smagorinsky closure for the deviatoric part, and the subgrid kinetic energy, computed by the dynamic procedure, for the isotropic part.

The near wall scaling of the dynamic Smagorinsky model is incorrect except for τ_{12} and τ_{23}, which are the critical components. Furthermore, it is reported in the literature that dynamic models can be very sensitive to the test filtering procedure and the stabilization method. Indeed, we have observed this same effect (incorrect near-wall scaling of the SGS stress tensor) in our channel flow simulations. The modeled heat flux tensor inherits its scaling from near-wall behavior of the stress tensor. Hence it becomes small, but not with the theoretical y_+ scaling. However, it has been verified that the eddy diffusivity becomes orders of magnitude less than the molecular diffusivity in the near-wall region ($y+ < 5$), as shown in Fig. 5. Incorrect scaling is not desirable, but it has a small effect, as long as the eddy diffusivity becomes small where it should.

III. NUMERICS, TEST CASES, AND RESULTS

The proposed model was tested after implementing it in the open source code OpenFOAM [22,23]. Gaussian finite volume integration, with a second order accurate, central differencing

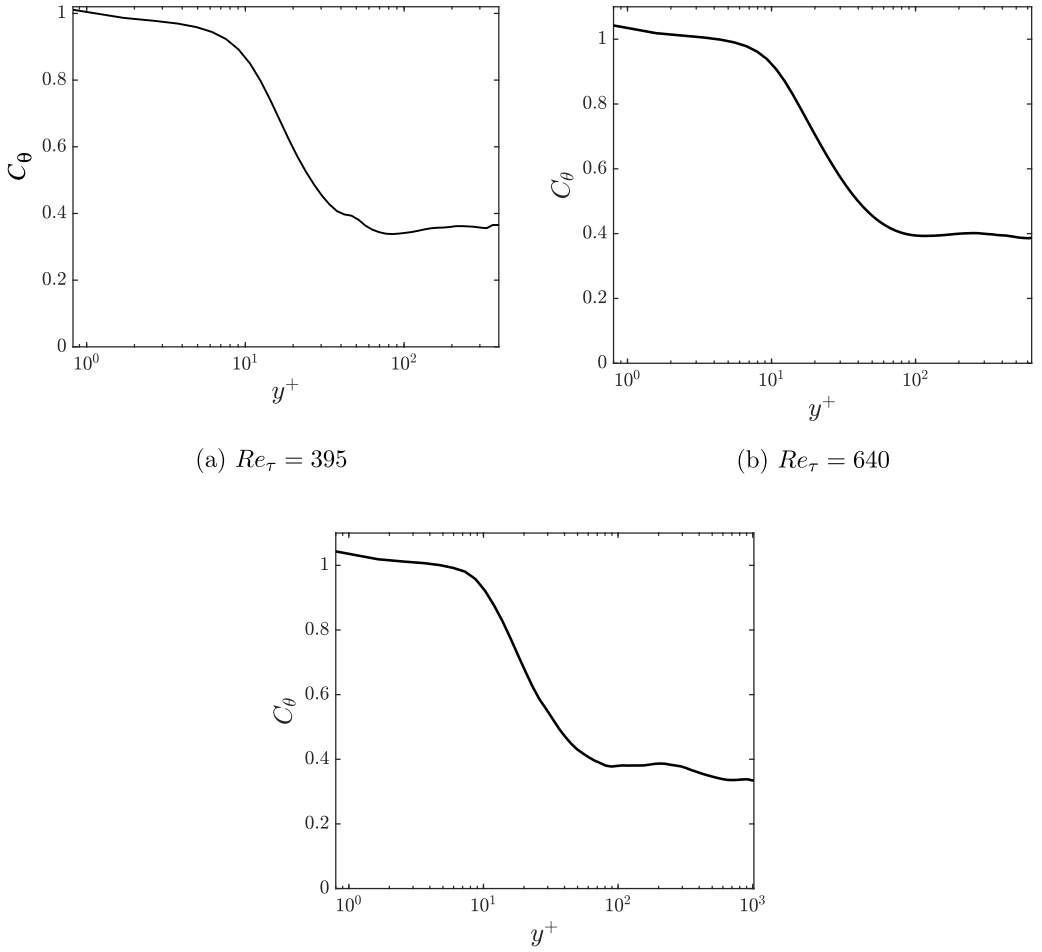

(a) $Re_\tau = 395$ (b) $Re_\tau = 640$

(c) $Re_\tau = 1020$

FIG. 3. Averaged model coefficients in fully developed turbulent channel flow at various Re_τ.

scheme was used for spatial discretization of the gradient and divergence terms in the governing equations. For convection of the passive scalar, the third order accurate flux interpolation scheme, QUICK, was chosen. A second order accurate, implicit scheme was chosen for temporal discretization. The pressure and momentum equations were solved by the generalized geometric-algebraic multigrid method and the symmetric Gauss-Seidel method, respectively. The PISO algorithm was used to solve the pressure and momentum equation correctors two times in each step.

A. Turbulent Poiseuille flow

An incompressible, pressure-driven, fully developed turbulent channel flow is considered for validation of the proposed model. The geometry of the computational domain which has dimensions $(L_x, L_y, L_z) = (6.4\delta, 2\delta, 3.2\delta)$ is shown in Fig. 6. The Reynolds number of the flow is $\mathrm{Re}_\tau = u_\tau \delta/\nu = 395$ and the molecular Prandtl number is chosen as $\mathrm{Pr} = 0.71$. Here, δ is the half-channel width and u_τ represents the wall-friction velocity. Two coarse grids, $G1$ and $G2$, with resolutions sufficient for a feasible LES have been used to validate the model and to examine the importance of SGS effects. The grids are uniformly spaced in the streamwise and spanwise directions, and

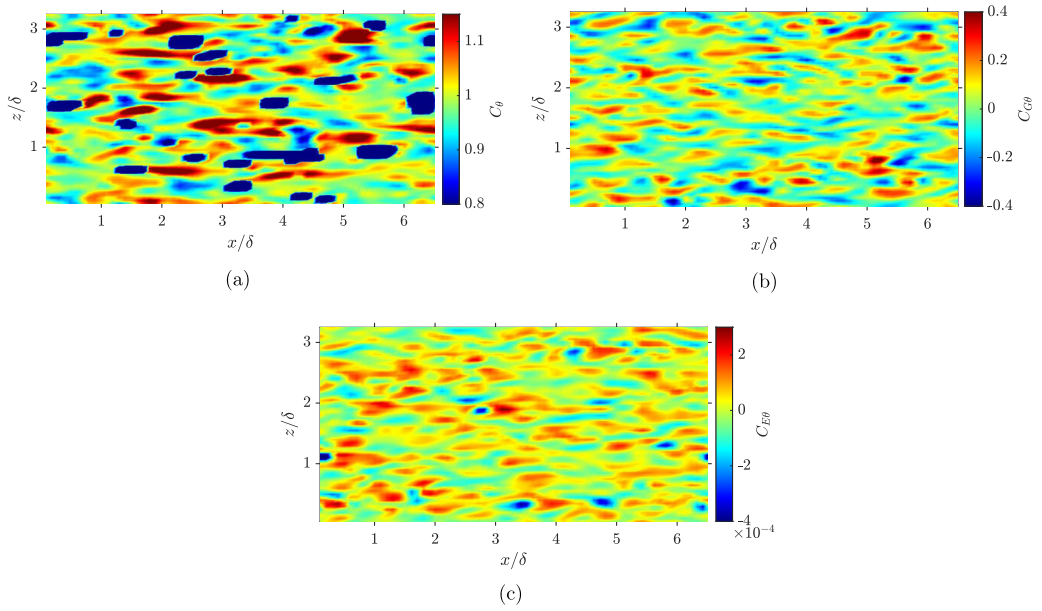

FIG. 4. Contours of instantaneous model coefficient at $y^+ = 5$ for present model (a), Dyn-GGDH (b), and Dyn-EDM (c). The results are shown for fully developed turbulent channel flow at $\mathrm{Re}_\tau = 395$.

stretched in the wall normal (y) direction by r_{exp}, the cell-to-cell expansion ratio. The grid details are summarized in Table I.

The boundary conditions are all set to periodic in streamwise and spanwise directions. The top and bottom walls are no slip for velocity, with a fixed gradient (constant heat flux) for the scalar (temperature) field. The mean momentum and temperature are held constant with respect to time by adding source terms to the momentum and scalar transport equations. From here on, "scalar" and "temperature" will be used interchangeably. It is to be noted that these grids are not overly fine, so that the SGS model plays a role in the velocity and scalar field solutions. To confirm that the numerical dissipation is not dominant in our test cases, the results obtained by the proposed model are compared in Fig. 7, with the LES without subgrid model for the fluxes. It is clear that the predictions from simulations with no SGS flux model are poorer in comparison to those obtained with the proposed model. This shows that the dissipation introduced by the model is greater than the numerical dissipation. The rms value of the scalar concentration is defined by $\theta'^{+}_{\mathrm{rms}} = [\{(\overline{\theta} - [\overline{\theta}])/\theta_\tau\}^2]^{1/2}$, where $[\cdot]$ represents the time average. The wall-friction temperature θ_τ is defined in Eq. (18).

The viscosity ratio for both the grids used is shown in Fig. 8. The considered Reynolds number is small, which may be why the averaged SGS viscosity is low compared to the molecular viscosity. However, instantaneous SGS viscosity ratios as high as 10 were observed in the simulations. In subsequent sections, we will show that the model delivers promising results in moderately high Reynolds number flows, as well as in separating flows on relatively coarser grids, with the viscosity ratios as high as 2–4. Also, as we will discuss, the effect of the proposed model is observed to be significant, even in an averaged sense.

1. Resolved velocity and scalar fields

Before analyzing the SGS effects of the proposed scalar-flux model, resolved fields are considered. In this section, both the velocity and the scalar fields will be presented.

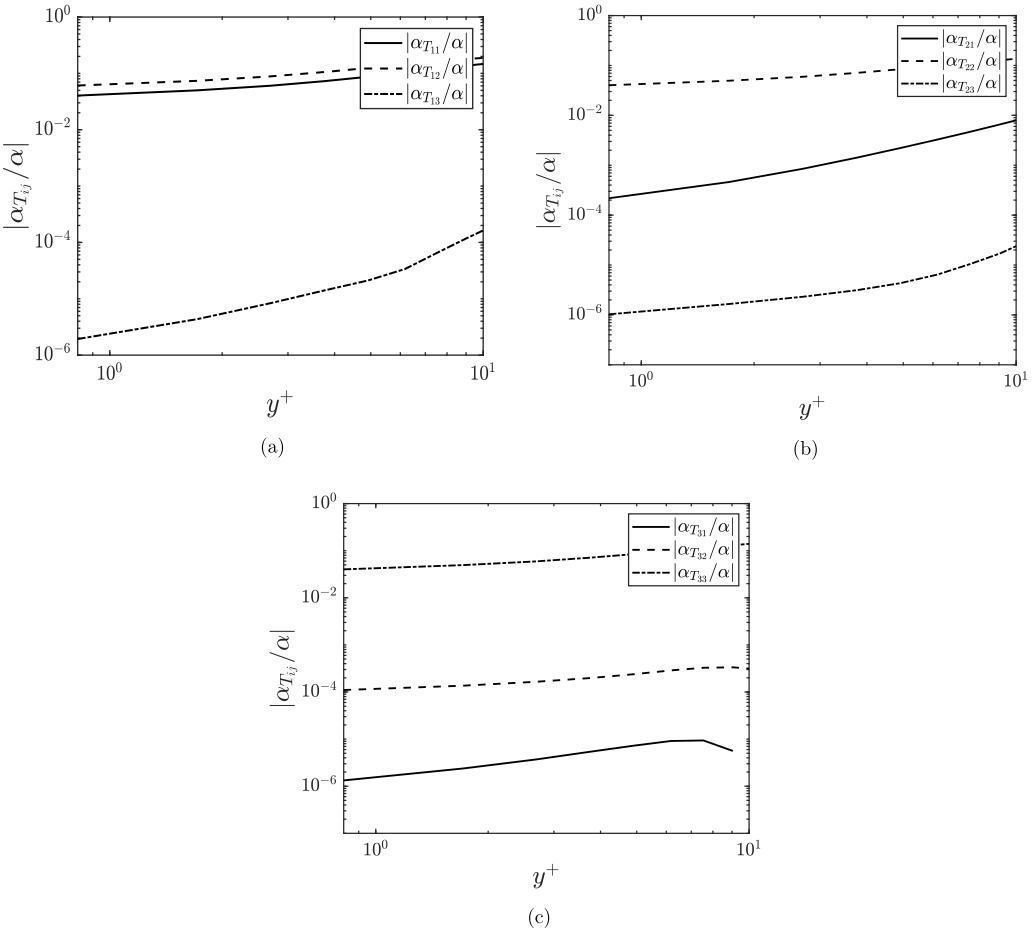

FIG. 5. Relative magnitude of eddy diffusivity components and molecular diffusivity at $y^+ < 10$ for the present model. The results are shown for fully developed turbulent channel flow at $\mathrm{Re}_\tau = 395$.

Figure 9(a) shows the predictions of the standard root-mean-square deviations of all the three components of the velocity in the wall normal, y, direction and Fig. 9(b) shows the mean streamwise velocity. The rms values of the resolved velocity are defined by

$$u'^{+}_{i,\mathrm{rms}} = [\{(\overline{u}_i - [\overline{u}_i])/u_\tau\}^2]^{1/2},$$

where $[\cdot]$ represents the time average. The predictions are compared for G1 with the DNS results of Moser *et al.* [24].

Although grid G1 is the finer of the two grids, it is still moderately coarse, considering the standard resolution requirements for a proper wall-resolved LES of channel flow. The wall-normal and spanwise components of the rms velocity fluctuations are slightly underpredicted, while the streamwise component has a higher peak followed by a region of underprediction closer to the core of the channel. Despite these slight inaccuracies in the rms values, the grid G1 is fine enough to produce a reasonably accurate mean velocity profile [Fig. 9(b)] suitable for testing the model for passive scalar advection.

The resolved streamwise and wall-normal heat fluxes are shown in Fig. 10(a), and the mean temperature profile is compared to DNS of Kawamura *et al.* [25] in Fig. 10(b). The fluxes and the

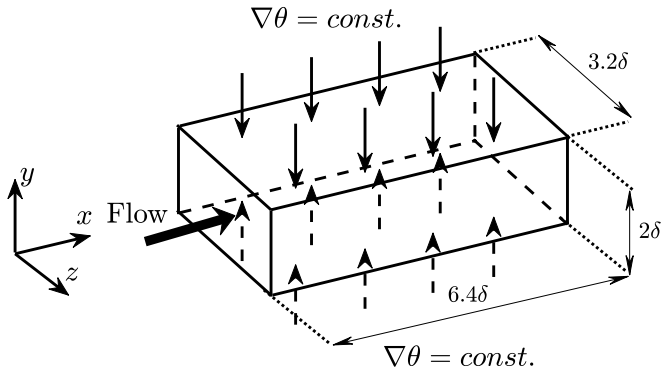

FIG. 6. Schematic of the flow domain and boundary conditions for fully developed channel flow.

temperature profile are normalized by wall-friction velocity, u_τ, and the wall-friction temperature,

$$\theta_\tau = \frac{\alpha}{u_\tau}\frac{\partial\overline{\theta}}{\partial y}\bigg|_w, \tag{18}$$

where α is the molecular diffusivity and the subscript w denotes the quantity computed at the wall. The temperature profile is plotted as

$$\overline{\theta}^+ = \frac{\overline{\theta}_w - \overline{\theta}(y)}{\theta_\tau}, \tag{19}$$

where $\overline{\theta}_w$ is the mean resolved wall temperature. Figure 11 shows this scaled temperature at two higher Reynolds numbers on the grids with resolution the same as G1. The mean temperature predictions are excellent.

To highlight the effect of modeling the SGS scalar fluxes, in Fig. 10(b), the resolved mean temperature prediction of the proposed model is compared with those of Dyn-EDM and Dyn-GGDH. It is observed that the prediction of the wall-normal distribution of the mean temperature by the proposed model is more accurate than the others, especially in the logarithmic layer. It is important to note here that the present model reverts back to Dyn-GGDH if the velocity gradient term (5) is neglected. Hence it is clear that the contribution of this term is very important in improving the resolved mean temperature predictions. Furthermore, this confirms that there is no physical reason for the diffusivity tensor to be symmetric.

To examine the validity of the current LES and to investigate the efficiency of the proposed SGS scalar-flux model, it is reasonable to look at the scalar energy balance across the channel. The fluxes are normalized by the viscous heat flux at the wall. Figure 12 shows the heat flux budget. The total heat flux consists of the contributions from the resolved viscous fluxes, resolved turbulent fluxes, and the subgrid fluxes, and varies approximately linearly across the channel with respect to the

TABLE I. Grid details for fully developed turbulent channel flow validation cases.

Case	$(N_x \times N_y \times N_z)$	Δx^+	Δz^+	r_{exp}
G1	$(64 \times 88 \times 64)$	40	20	1.09
G2	$(44 \times 68 \times 44)$	60	30	1.125

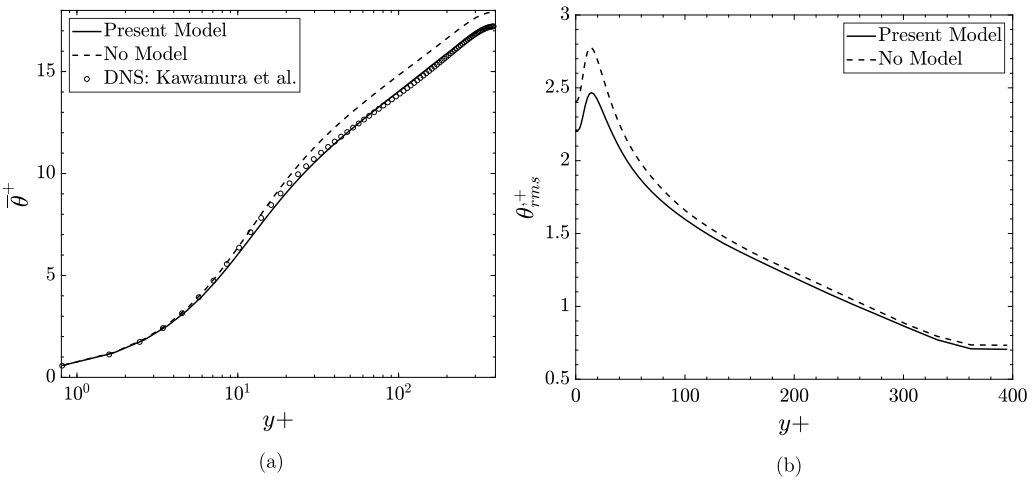

FIG. 7. Mean resolved temperature (a) and resolved scalar fluctuations (b) for grid G1 with and without the subgrid model.

wall-normal coordinate normalized by wall units,

$$q^+_{\text{total}} = \frac{1}{\text{Pr}}\frac{\partial \overline{\theta}^+}{\partial y^+} - \overline{v'^+\theta'^+} - h^+_{y\theta} \approx 1 - \frac{y^+}{\text{Re}_\tau}. \tag{20}$$

It is evident from Fig. 12 that the total computed heat flux is close to the theoretical linear variation. An instantaneous SGS heat flux at $x/L_x = z/L_z = 0.5$ is also shown. Although the time and span averaged SGS heat flux is relatively small, the magnitude of the local and instantaneous value is observed to be appreciable.

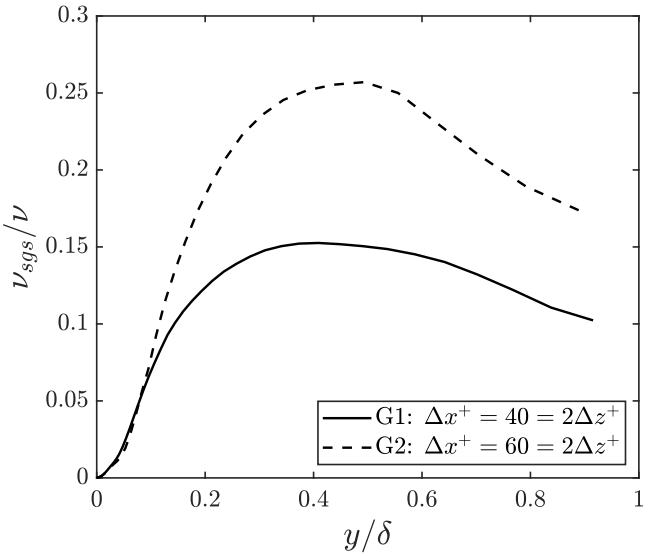

FIG. 8. Time averaged SGS viscosity compared to the molecular one for fully developed channel flow.

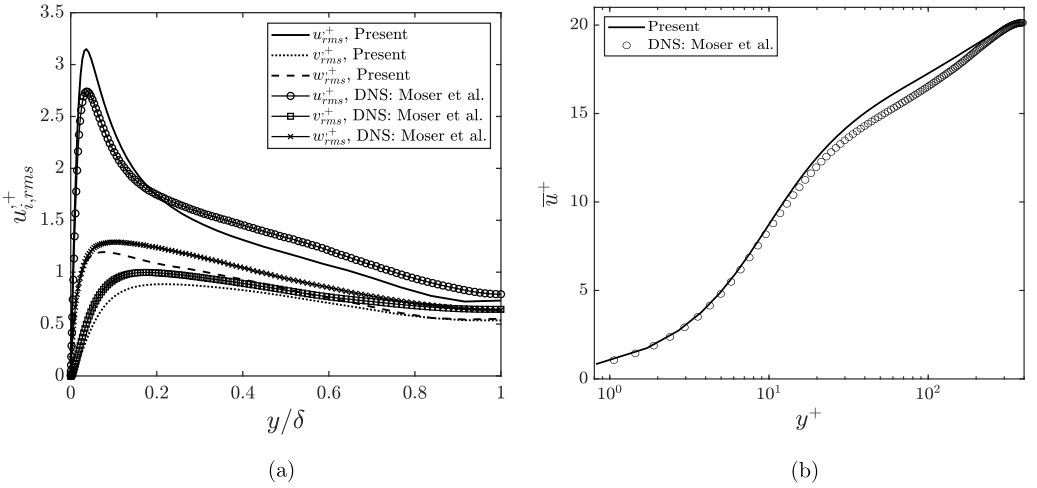

FIG. 9. Resolved velocity fluctuations (a) and resolved mean streamwise velocity (b) for grid G1.

2. Subgrid scalar-flux structure

The previous subsection focused mainly on the resolved quantities associated with the velocity and scalar fields. To evaluate the effectiveness of the proposed tensor diffusivity model at the subgrid scale, it is important to quantify the SGS effects. Some studies [11] have recommended characterizing the SGS scalar-flux model by the magnitude of the effective diffusivity and by the alignment between the SGS scalar flux and the resolved temperature gradient. In this subsection, we will examine such quantities for the proposed model, in comparison with the Dyn-EDM and Dyn-GGDH models. The asymmetry in the diffusion tensor and relative magnitude of the streamwise and wall-normal fluxes will also be discussed.

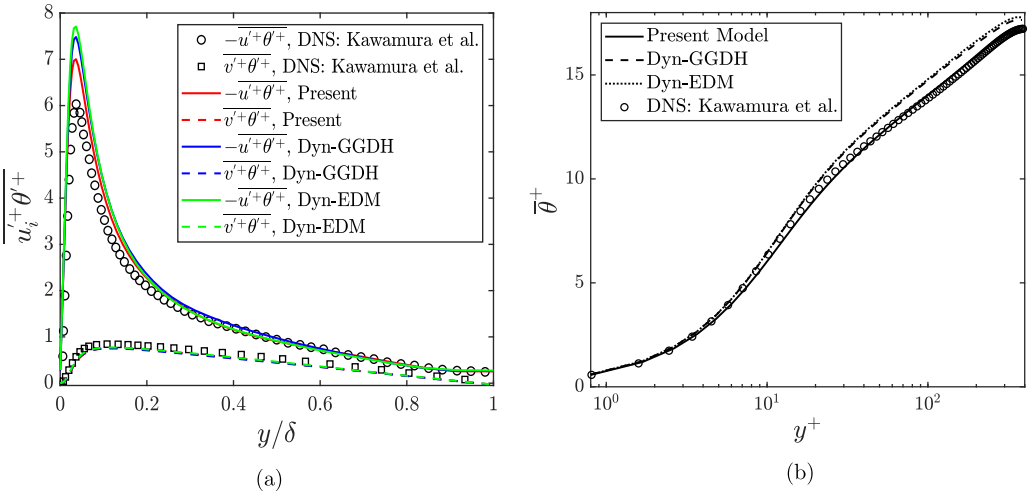

FIG. 10. Resolved streamwise and wall-normal heat fluxes (a) and mean resolved temperature (b) for grid G1.

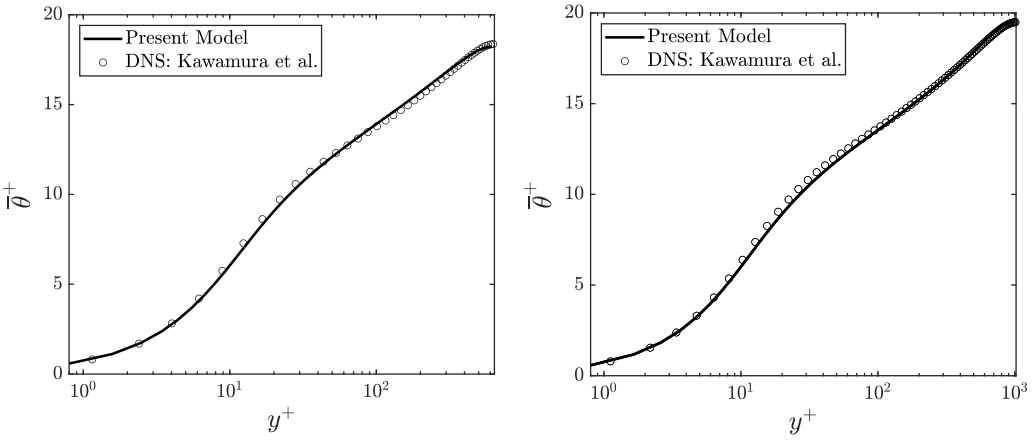

(a) $Re_\tau = 640$ (b) $Re_\tau = 1020$

FIG. 11. Mean temperature at $\mathrm{Re}_\tau = 640$, 1020.

The alignment angle Φ between the resolved temperature gradient and the modeled SGS heat flux is

$$\Phi = \cos^{-1}\left(\frac{h_{i\theta}\cdot\overline{\theta}_{,i}}{|h_{i\theta}||\overline{\theta}_{,i}|}\right). \tag{21}$$

Figure 13 shows the PDF of the instantaneous alignment angle predicted by the Dyn-EDM, Dyn-GGDH, and the present model. Negative values of the model coefficients have been allowed for all of the described models. It is evident in Fig. 13(a) that Φ predicted by the Dyn-EDM is either 0° or 180° corresponding to $C_{E\theta} < 0$ or $C_{E\theta} > 0$, respectively. The predictions are similar in the regions near the wall ($y^+ = 3$) and near the center of the channel ($y^+ = 350$). As the physical mechanism of heat transfer at the subgrid scale is significantly different from the simple gradient

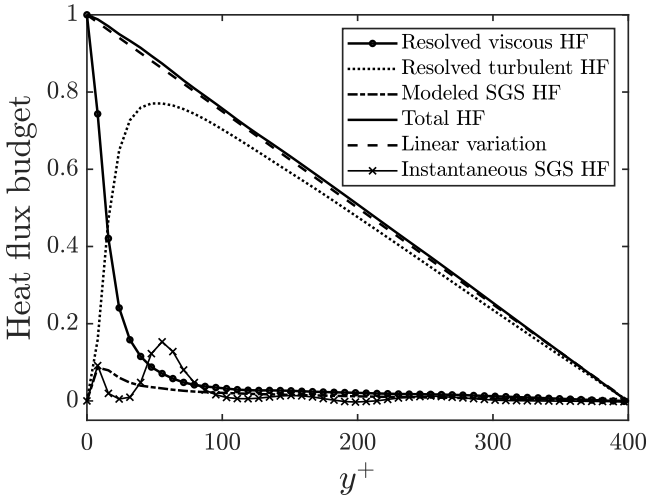

FIG. 12. Normalized heat-flux budget in the wall-normal direction on grid G1 for fully developed channel flow.

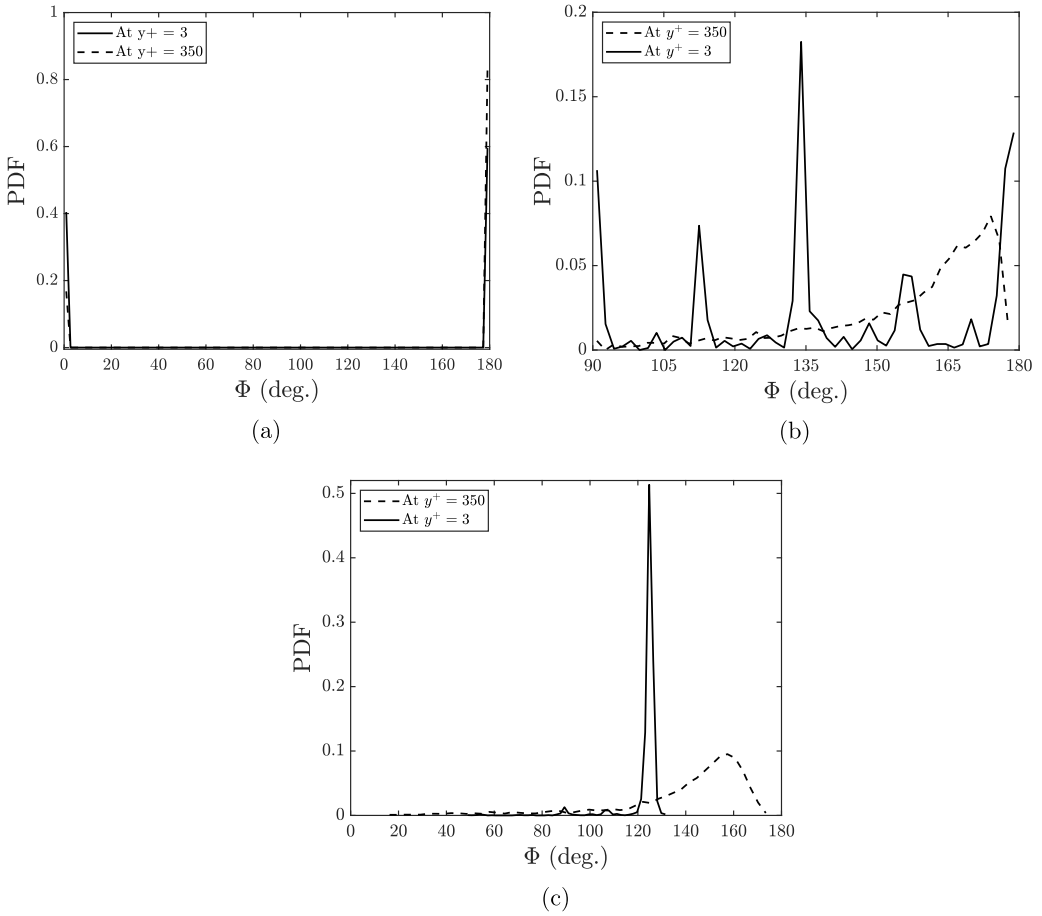

FIG. 13. PDF of the alignment angle between the resolved temperature gradient and the SGS heat flux for Dyn-EDM (a), Dyn-GGDH (b), and the proposed model (c). The results are shown for fully developed channel flow on grid G1.

diffusion constitutive relation, the Dyn-EDM fails to accurately describe the physics of heat transfer at such scales.

Tensor diffusivity models, however, are able to predict a SGS heat flux vector which is rotated with respect to the temperature gradient, giving rise to a wide range of alignment angles. In the case of Dyn-GGDH, as shown in Fig. 13(b), the PDF of the instantaneous alignment angle is quite scattered with a substantial contribution from $\Phi = 180^\circ$. The near wall predictions are better than those away from the wall.

In the proposed SGS heat flux model, Fig. 13(c), a single angle of $\Phi \approx 125^\circ$ is preferred in the near wall region. This property is in accordance with the physical intuition that, in the near wall region, the direction of the flux is governed by both the wall-normal temperature gradient and the advection of temperature parallel to the wall, giving rise to the SGS heat flux vector aligned at the angles weighted toward $\Phi = 90^\circ$. In the core region of the channel, the proposed model predicts Φ closer to 150°, which is still better than both the Dyn-EDM and Dyn-GGDH model predictions.

In order to compare the SGS effects of tensor diffusivity models with the Dyn-EDM, it is reasonable to define the effective SGS diffusivity as

$$\alpha_{\text{sgs}}^{\text{eff}} = -h_{2\theta}/(\partial\overline{\theta}/\partial y). \tag{22}$$

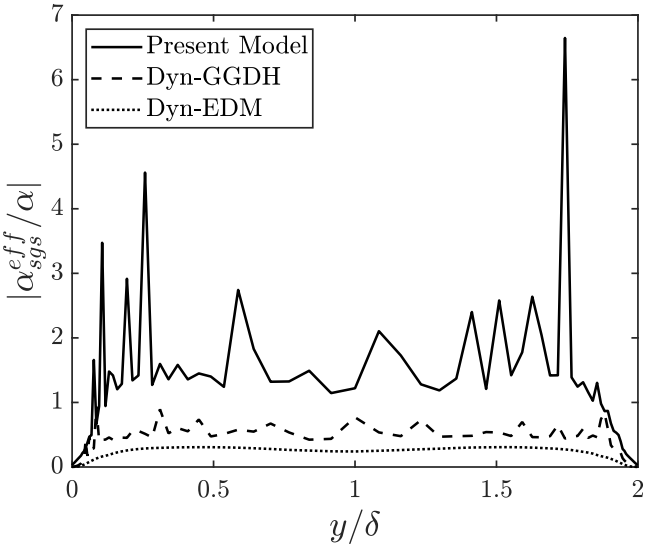

FIG. 14. Effective SGS diffusivity for Dyn-EDM, Dyn-GGDH, and the proposed model.

The ratio of the averaged effective SGS diffusivity to the molecular diffusivity is quantified for all three models in Fig. 14. This ratio signifies how important the SGS diffusion is, compared to molecular diffusion. It is observed that the degree of variability in the effective SGS diffusivity is greatest in the case of the proposed model. The value of $\alpha^{\text{eff}}_{\text{sgs}}/\alpha$ predicted by Dyn-EDM and Dyn-GGDH models ranges from zero at the wall to a maximum of $\approx$0.4 and $\approx$0.9 in the core region, respectively. However, the effective diffusivity of the present model is close to 1.5 over most of the channel and has a maximum of about 6.5. It is to be noted that, in the case of the Dyn-EDM, diffusivity is expressed simply by a scalar α_T and there is no question of defining an effective diffusivity.

The effectiveness of any SGS heat flux model is best gauged by how well it can represent the geometrical structure of the fluxes at subgrid level. Considering the case of resolved fluxes, it is evident that the magnitude of streamwise fluxes is always greater than the magnitude of wall-normal fluxes, i.e., $|\overline{u'\theta'}| > |\overline{v'\theta'}|$; see Fig. 10(a). A good SGS heat flux model should be able to preserve this structure for the SGS heat fluxes, i.e., $|h_{1\theta}| > |h_{2\theta}|$.

From Fig. 15(a), it is clear that the Dyn-EDM fails to produce a streamwise heat flux. Figure 15(b) displays the SGS heat flux structure predicted by the Dyn-GGDH and the proposed model. Although Dyn-GGDH is able to predict the streamwise fluxes slightly better than the Dyn-EDM, it yields $|h_{1\theta}^{+\text{GGDH}}| < |h_{2\theta}^{+\text{GGDH}}|$, which is not in agreement with the structure of fluxes prescribed by the resolved scales. The present model generally predicts a larger magnitude of the streamwise and wall-normal fluxes than those of the Dyn-EDM and Dyn-GGDH models, and it also successfully preserves the correct geometrical structure of the fluxes with $|h_{1\theta}^{+\text{present}}| > |h_{2\theta}^{+\text{present}}|$.

The diffusivity tensor, $\alpha_{T_{ij}}$, given by Eq. (8) consists of the contributions from the SGS stress which is symmetric and from the shear rate which is asymmetric. Thus $\alpha_{T_{ij}}$ can be written as the sum of a symmetric part and an asymmetric part,

$$\alpha_{T_{ij}} = \alpha^S_{T_{ij}} + \alpha^A_{T_{ij}}, \tag{23}$$

where $\alpha^S_{T_{ij}} = C_\theta \mathscr{T} \tau_{ij}$ and $\alpha^A_{T_{ij}} = -C_\theta \mathscr{T} \alpha^*_{T_{kj}} \partial \overline{u}_i/\partial x_k$. Averaged values of the normalized diffusivity tensor components for the present model are shown in Fig. 16. From Fig. 16(a), it is clear that the model captures anisotropy of the diffusivity tensor. The model is also able to reproduce the

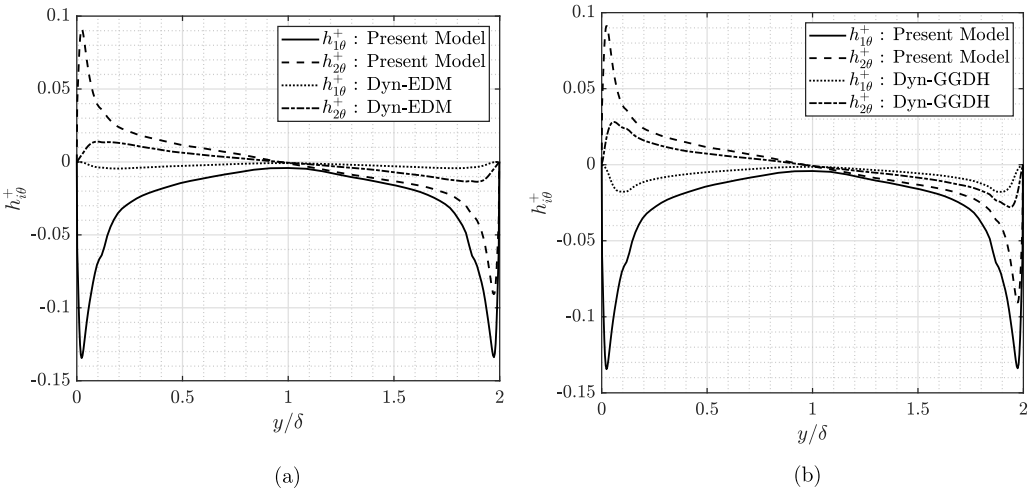

FIG. 15. Comparison of time and span averaged SGS heat fluxes in streamwise and wall-normal direction between Dyn-EDM (a), Dyn-GGDH (b), and the proposed model. The values of normalized by friction velocity and friction temperature.

expected asymmetry, $\alpha_{T_{12}} \ll \alpha_{T_{21}} < 0$, in Fig. 16(b). The asymmetry in the diffusivity tensor is due to the contribution of the velocity gradient to flux production.

3. Grid G2 predictions

Grid G2 is the coarser of the two grids used. Figure 17(a) displays the ratio $\alpha^{\text{eff}}_{\text{sgs}}/\alpha$. Evidently, for the proposed model, on a coarse grid the ratio becomes large and goes as high as 18. It is interesting to note that diffusivities of the Dyn-EDM and Dyn-GGDH models are still small in comparison with the molecular value. Although the SGS effects predicted by the proposed model are larger on grid G2, it nevertheless yields a reasonably accurate mean temperature profile as shown in Fig. 17(b). The Dyn-EDM and Dyn-GGDH models are observed to be unsuccessful in doing that. Since the

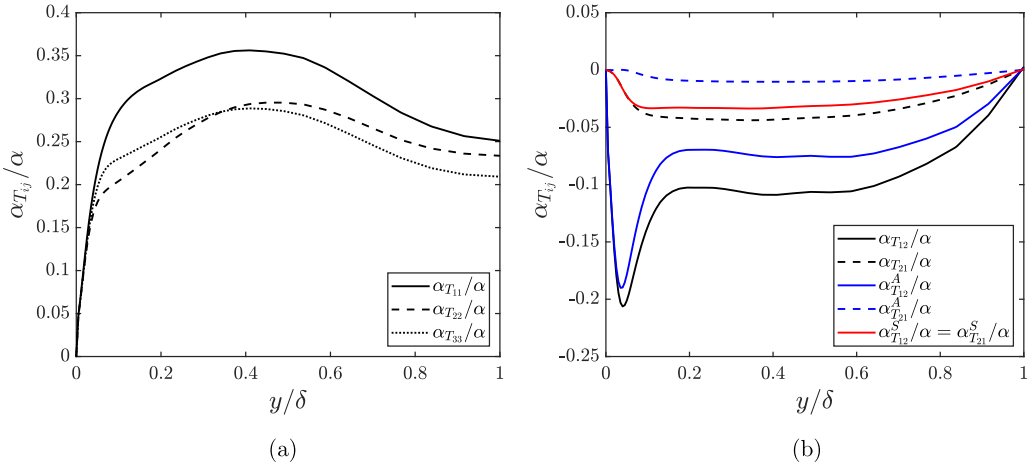

FIG. 16. Anisotropy (a) and asymmetry (b) of the model diffusivity tensor, $\alpha_{T_{ij}}$, for the present model.

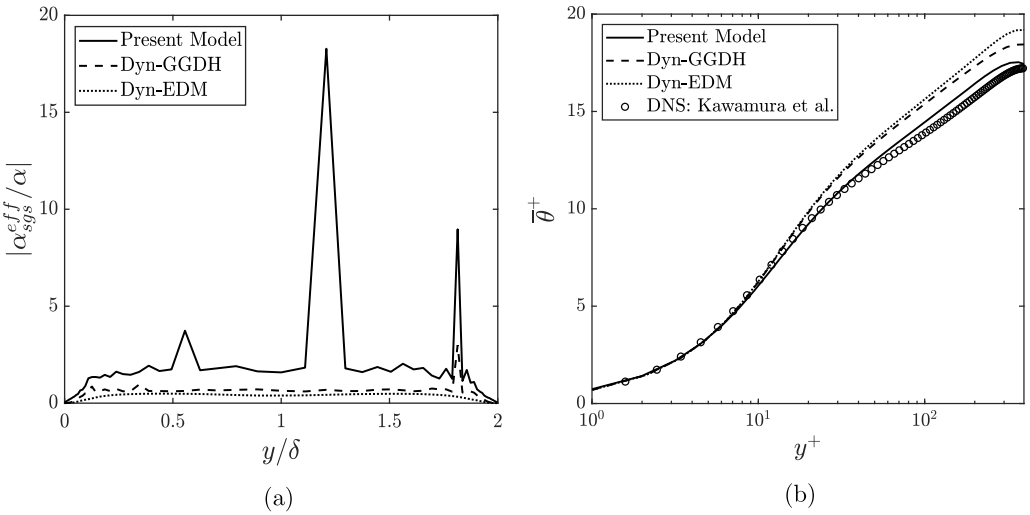

FIG. 17. Ratio of the averaged absolute effective diffusivity and molecular diffusivity (a) and mean resolved temperature (b) predictions on grid G2 by different models.

mean temperature profiles for both the grids G1 and G2 are reasonably close to the DNS data, they serve to show a capability of the model to reduce mesh insensitivity.

4. Numerical efficiency

Table II lists the normalized computational time (with respect to that of Dyn-EDM) of all the considered models at various Reynolds numbers for the plane channel flow. The flow was computed for a fixed time of 60, 40, and 20 flow through times for $\mathrm{Re}_\tau = 395$, 640, and 1020, respectively, with the appropriate number of processors, which was kept constant for the same Re_τ. It can be seen that the proposed model incurs about 20% additional cost with respect to the Dyn-EDM model for almost all of the Reynolds numbers. Keeping in mind that the solutions derived from Dyn-GGDH and Dyn-EDM were not accurate, an increase of 10–20% in computational cost with respect to Dyn-GGDH and Dyn-EDM models, respectively, is justifiable.

B. Flow and heat transfer over a backward facing step

It is important to test the performance of the model in a flow with separation. Separated and reattaching flows with heat transfer are of practical interest in nuclear reactors, gas turbines, and electronic circuits. Here we consider the well studied case of the flow over a backward facing step with heat transfer downstream of the step.

The simulation is of the reference case in Adams *et al.* [26] and Vogel and Eaton [27]. A schematic of the simulation domain and the grid are shown in Fig. 18. The dimensions of the domain are $(22H \times 5H \times 3H)$ with an entrance length of $2H$, upstream of the step. The grid consists of

TABLE II. Computational cost comparison of the proposed model with Dyn-GGDH and Dyn-EDM models.

Re_τ\Model	Present	Dyn-GGDH	Dyn-EDM
395	1.22	1.05	1.00
640	1.24	1.06	1.00
1020	1.20	1.10	1.00

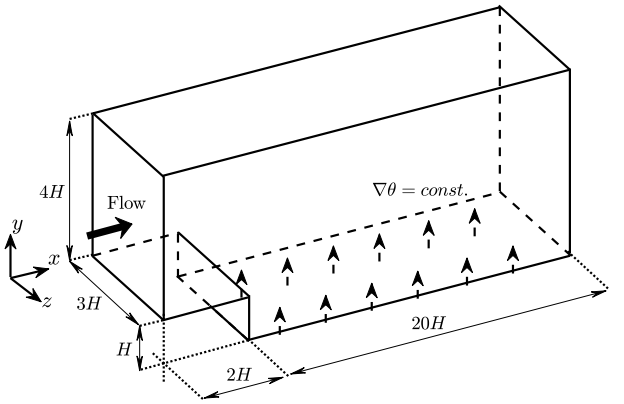

(a)

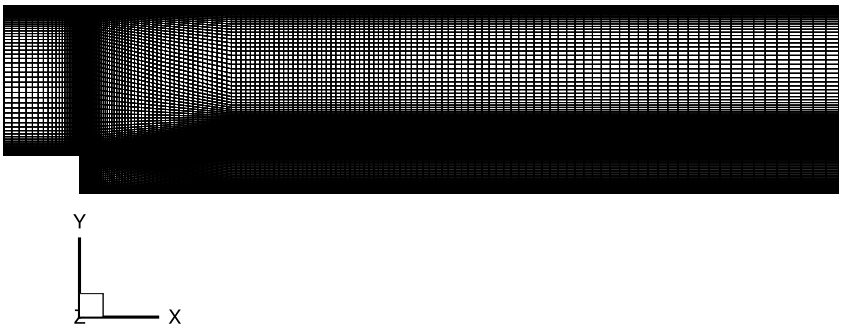

(b)

FIG. 18. Computational domain (a) and the grid used (b) for the backward facing step simulations.

144×96 nodes in streamwise and spanwise directions, downstream of the step. The grid is stretched in the wall normal, as well as the streamwise direction, away from the step, as evident in Fig. 18(b). In wall units of the upstream boundary layer, the grid resolution at some pivotal locations in the domain are

$$\Delta x^+_{\text{min}} = 15, \quad \text{at the step,}$$
$$\Delta x^+_{\text{max}} = 450, \quad \text{at the exit boundary,}$$
$$\Delta z^+ = 42.5, \quad \text{uniform in span,}$$
$$\Delta y^+_{\text{min}} = 1.0, \quad \text{at all the walls.}$$

Let it be reiterated here that the grid is coarse, as the ratio of subgrid to molecular viscosity was observed to be as high as 2.5 over almost all of the domain. The Reynolds number based on the step height is $\text{Re}_H = 28\,000$ and the expansion ratio of the channel at the step is 1.25. The molecular Prandtl number is $\text{Pr} = 0.71$. The boundary conditions are all set to periodic in the spanwise direction. For the temperature field, a constant heat flux of 270 W/m^{-2} is prescribed on the lower wall, downstream of the step. The inflow condition consists of an inlet boundary layer on both the top and bottom walls, upstream of the step, separated by a somewhat undisturbed core. The inlet boundary layers for the reference case are described by the momentum thickness Reynolds number $\text{Re}_\Theta = 3370$ and a measured thickness of $\delta/H = 1.1$. At the exit, the boundary condition on velocity and temperature fields is set to zero gradient.

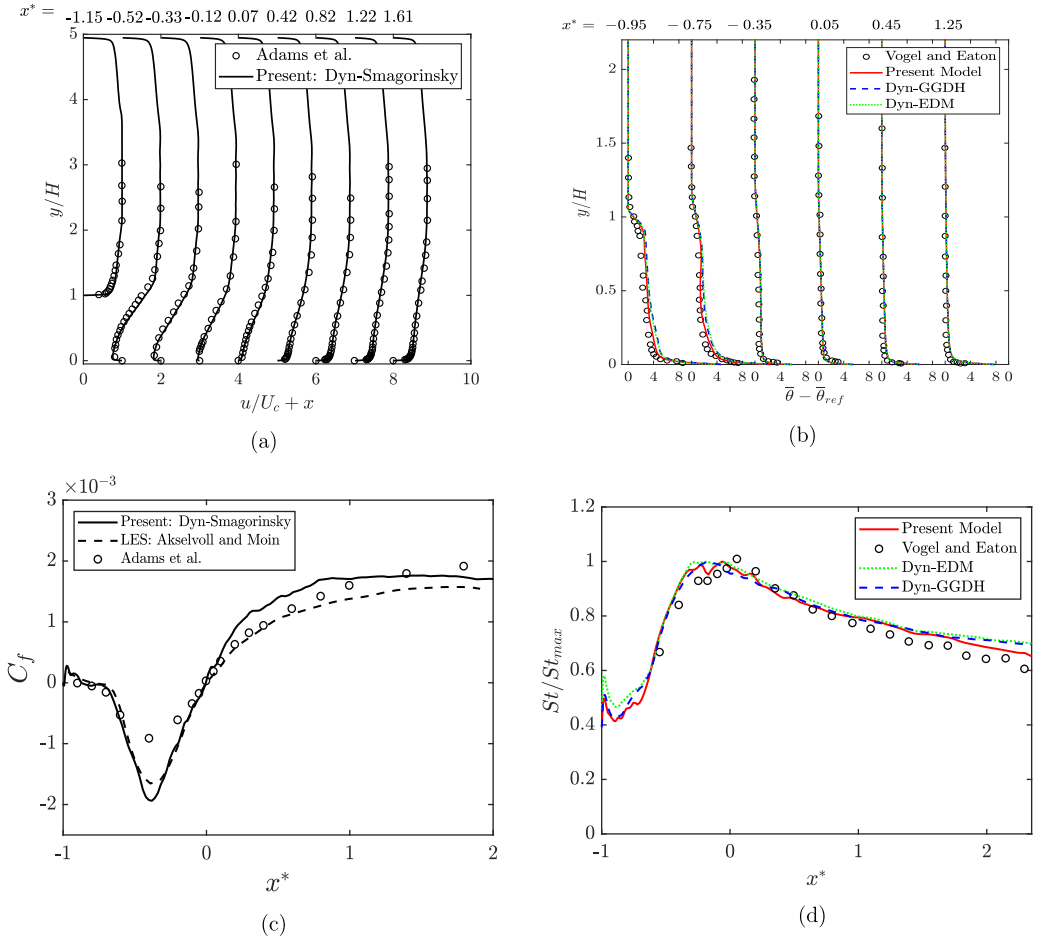

FIG. 19. Mean velocity (a), mean temperature (b), skin friction coefficient (c), and Stanton number (d) profiles along the lower wall downstream of the step.

A precursor channel flow simulation ($3.3H \times 4H \times 3H$) was calculated to generate the upstream boundary layer flow by rescaling and recycling the boundary layer near the outlet of the channel back to the inlet. Then the turbulent boundary layer was mapped from the channel exit to the inlet of the backstep domain. Care has been taken to match the inlet turbulent boundary layer to that of the experiments. However, certain discrepancies still exist due to the short length of the precursor simulation; thus it was not possible to exactly simulate the upstream boundary layer. This might possibly affect the accuracy of the simulation results. However, it has been shown by Westphal *et al.* [28] that, if the renormalized coordinate $x^* = (x - x_r)/x_r$ is used, where x_r is the mean reattachment length, statistical data are quite insensitive to the inflow conditions. This has been observed by various researchers in LES of the backward-facing step.

The mean velocity, skin friction coefficient, mean resolved temperature, and Stanton number predictions are shown in Fig. 19. The mean profiles of velocity and temperature, predicted by the proposed model, are reasonably accurate and match well with the experimental results of Vogel and Eaton [27]. The mean temperature profile is compared with the predictions of Dyn-GGDH and Dyn-EDM models in Fig. 19(b). The results are nearly identical far downstream of the step, but near the location of the step the proposed model predicts a better agreement with the experiments. However, the proposed model slightly overpredicts the wall temperature, which is seen with other

models, too. The near wall temperature data from the experiment is not reliable and some data points have been ignored for clarity. From Fig. 19(c), it can be observed that, in the recirculation zone, the LES results show a larger negative value of C_f. It is not clear why the LES overpredicts the magnitude of C_f, but the same inaccuracy has been reported by Keating *et al.* [29] and Akselvoll and Moin [30]—as depicted in Fig. 19(c). The reason for the poor agreement in the skin-friction coefficient could be attributed to the inflow generation method and/or to inadequate grid resolution in this region. However, Keating *et al.* [29] used a finer grid and did not see any improvements in the C_f. Another cause might be the limited spanwise extent of the domain; but, preliminary studies by Keating *et al.* [29] with wider domains did not improve the results.

The wall heat transfer characteristics predicted by the proposed heat flux model are quantified by the Stanton number in Fig. 19(d). The Stanton number profile matches well with the experimental data. The Stanton number predictions of Dyn-EDM and Dyn-GGDH differ from those of the proposed model near the step location and far downstream where the mesh is coarse. For the rest of the domain, the profiles are somewhat similar. The contrast, that St matches well with the experimental data, while C_f does less so, is probably because of different mechanisms that are responsible for heat and momentum transfer, as evidenced by the breakdown of Reynolds' analogy in the recirculation zone.

IV. CONCLUSIONS

In this work, a dynamic SGS scalar-flux model is proposed which is based on the exact rate of production of turbulent fluxes. The model incorporates a tensor diffusivity with explicit dependence on the subgrid stresses and the resolved velocity gradient. The fact that the diffusivity is represented by a tensor allows the scalar-flux vector to be misaligned with the filtered temperature gradient.

Some numerical challenges were faced in representing the fluxes by the explicit formula, Eq. (6)—i.e., stiffness and unphysicality of the solution. To overcome these issues, the flux term on the RHS of Eq. (8) is updated explicitly. Then the model coefficient is computed dynamically.

To validate the model, predictions were compared to DNS data in channel flow and to the predictions by the Dyn-EDM and Dyn-GGDH models. It was shown that the prediction of the mean resolved temperature (on two coarse grids) is better than these other two models. The proposed model is observed to correctly predict the relative magnitude of wall-normal and wall-tangential flux and the PDF of the instantaneous alignment angle between turbulent flux and temperature gradient.

It is noteworthy that the subgrid to molecular diffusivity ratio was much larger than those of the Dyn-EDM and Dyn-GGDH models; so the improved predictions are due to a greater reliance on the subgrid model. While it is not entirely deductive, it can be presumed that adopting the exact flux production term into the model, and accepting that it produces an asymmetric diffusion tensor, as exemplified by Fig. 16, are useful properties of the formulation. The larger value of the model coefficient, C_θ, and especially its rise near the wall, also contrasts to the comparison models. The free index in Eq. (9) contains a contribution from the direction of the resolved velocity, rather than the direction of its gradient. Near the wall, where the velocity in the x direction is dominant, the streamwise flux will make a large contribution to Eq. (15), and that may explain the behavior of C_θ.

The results reflecting the performance of the proposed scalar-flux model at the subgrid scale are promising and its ability to correctly predict the near-wall heat transfer characteristics in a separated and reattaching flow is encouraging.

ACKNOWLEDGMENTS

This work was supported in part by the Office of Naval Research under Award No. N00014-17-1-2200. Computer time was provided by the Extreme Science and Engineering Discovery Environment (XSEDE).

APPENDIX

An estimate of the subgrid turbulent kinetic energy is based on the dynamic Smagorinksy model, as implementation by Passalacqua [31] for OpenFOAM. The SGS stress tensor $\tau_{ij} = \overline{u_i u_j} - \overline{u}_i \overline{u}_j$ is modeled by $\frac{2}{3} k_{\rm sgs} \delta_{ij} - 2\nu_{\rm sgs} \overline{S}_{ij}$, where

$$\overline{S}_{ij} = \frac{1}{2}\left(\frac{\partial \overline{u}_i}{\partial x_j} + \frac{\partial \overline{u}_j}{\partial x_i} \right).$$

The subgrid kinetic energy is the trace of the stress tensor, $k_{\rm sgs} = \tau_{kk} = (\overline{u_k u_k} - \overline{u}_k \overline{u}_k)$.

Let

$$\nu_{\rm sgs} = C_k \Delta \sqrt{k_{\rm sgs}}. \tag{A1}$$

Using a local equilibrium approximation that production equals dissipation, and representing dissipation by $C_\epsilon k_{\rm sgs}^{1.5}/\Delta$,

$$\overline{S} : \tau_{ij} = C_\epsilon \frac{k_{\rm sgs}^{1.5}}{\Delta} \Rightarrow C_\epsilon \frac{k_{\rm sgs}^{1.5}}{\Delta} = 2\nu_{\rm sgs} |\overline{S}|^2, \tag{A2}$$

where $|\overline{S}| = \sqrt{2\overline{S} : \overline{S}}$. Hence

$$k_{\rm sgs} = C_{\rm dyn} \Delta^2 |\overline{S}|^2. \tag{A3}$$

$C_{\rm dyn}$ is computed dynamically by using trace of the resolved stress tensor and modeled $k_{\rm sgs}$ at the test and grid level filters.

[1] M. Germano, Turbulence: The filtering approach, J. Fluid Mech. **238**, 325 (1992).

[2] P. Moin, K. Squires, W. Cabot, and S. Lee, A dynamic subgrid-scale model for compressible turbulence and scalar transport, Phys. Fluids A: Fluid Dyn. **3**, 2746 (1991).

[3] Z. Yin and P. A. Durbin, Passive scalar transport modeling for hybrid RANS/LES simulation, Flow Turbul. Combust. **98**, 177 (2017).

[4] P. A. Durbin and B. A. Pettersson-Reif, Advanced topics, in *Statistical Theory and Modeling for Turbulent Flows* (John Wiley & Sons, Ltd., New York, 2010), Chap. 8, pp. 217–248.

[5] S. Tavoularis and S. Corrsin, Experiments in nearly homogeneous turbulent shear flow with a uniform mean temperature gradient. part 1, J. Fluid Mech. **104**, 311 (1981).

[6] M. M. Rogers, N. N. Mansour, and W. C. Reynolds, An algebraic model for the turbulent flux of a passive scalar, J. Fluid Mech. **203**, 77 (1989).

[7] In boundary layers, a value of $Pr_T = 0.85$–0.90 is generally prescribed for RANS computations.

[8] B. J. Daly and F. H. Harlow, Transport equations in turbulence, Phys. Fluids **13**, 2634 (1970).

[9] B.-C. Wang, E. Yee, D. J. Bergstrom, and O. Iida, New dynamic subgrid-scale heat flux models for large-eddy simulation of thermal convection based on the general gradient diffusion hypothesis, J. Fluid Mech. **604**, 125 (2008).

[10] S.-H. Peng and L. Davidson, On a subgrid-scale heat flux model for large eddy simulation of turbulent thermal flow, Int. J. Heat Mass Transf. **45**, 1393 (2002).

[11] B.-C. Wang, E. Yee, J. Yin, and D. J. Bergstrom, A general dynamic linear tensor-diffusivity subgrid-scale heat flux model for large-eddy simulation of turbulent thermal flows, Numer. Heat Transfer, Pt. B **51**, 205 (2007).

[12] J. Bardina, J. Ferziger, and W. Reynolds, Improved subgrid-scale models for large-eddy simulation, in 13th Fluid and Plasma-Dynamics Conference, Snowmass, CO, 1980 (unpublished), https://arc.aiaa.org/doi/abs/10.2514/6.1980-1357.

[13] P. Sagaut, Coupling with passive/active scalar, in *Large Eddy Simulation for Incompressible Flows* (Springer, Berlin, Heidelberg, 2006), Chap. 15, pp. 449–493.

[14] M. V. Salvetti and S. Banerjee, *A priori* tests of a new dynamic subgrid-scale model for finite-difference large eddy simulations, Phys. Fluids **7**, 2831 (1995).
[15] G. Balarac, J. Le Sommer, X. Meunier, and A. Vollant, A dynamic regularized gradient model of the subgrid-scale scalar flux for large eddy simulations, Phys. Fluids **25**, 075107 (2013).
[16] H. Lu and F. Porté-Agel, A modulated gradient model for scalar transport in large-eddy simulation of the atmospheric boundary layer, Phys. Fluids **25**, 015110 (2013).
[17] Y. Shabany and P. A. Durbin, Explicit algebraic scalar flux approximation, AIAA J. **35**, 985 (1997).
[18] S. G. Chumakov, A priori study of subgrid-scale flux of a passive scalar in isotropic homogeneous turbulence, Phys. Rev. E **78**, 036313 (2008).
[19] U. Piomelli and J. Liu, Large-eddy simulation of rotating channel flows using a localized dynamic model, Phys. Fluids **7**, 839 (1995).
[20] B. A. Younis, C. G. Speziale, and T. T. Clark, A rational model for the turbulent scalar fluxes, Proc. R. Soc. London A **461**, 575 (2005).
[21] D. K. Lilly, A proposed modification of the Germano subgrid-scale closure method, Phys. Fluids A: Fluid Dyn. **4**, 633 (1992).
[22] H. Jasak, A. Jemcov, and Z. Tukovíc, Openfoam: A C++ library for complex physics simulations, in International Workshop on Coupled Methods in Numerical Dynamics, Dubrovnik, Croatia, 2007 (unpublished).
[23] H. G. Weller, G. Tabor, H. Jasak, and C. Fureby, A tensorial approach to computational continuum mechanics using object-oriented techniques, Comput. Phys. **12**, 620 (1998).
[24] R. D. Moser, J. Kim, and N. N. Mansour, Direct numerical simulation of turbulent channel flow up to $Re_\tau = 590$, Phys. Fluids **11**, 943 (1999).
[25] H. Kawamura, H. Abe, and Y. Matsuo, DNS of turbulent heat transfer in channel flow with respect to Reynolds and Prandtl number effects, Int. J. Heat Fluid Flow **20**, 196 (1999).
[26] E. W. Adams, J. P. Johnston, and J. K. Eaton, Experiments on the structure of turbulent reattaching flow, Report No. MD-43, Stanford Univ., Thermo-sciences Division, Department of Mechanical Engineering, 1984 (unpublished).
[27] J. C. Vogel and J. K. Eaton, Combined heat transfer and fluid dynamic measurements downstream of a backward-facing step, J. Heat Transfer **107**, 922 (1985).
[28] R. V. Westphal, J. P. Johnston, and J. K. Eaton, Experimental study of flow reattachment in a single-sided sudden expansion, Ph.D. thesis, Stanford Univ., Thermo-sciences Division, Department of Mechanical Engineering, 1983.
[29] A. Keating, U. Piomelli, K. Bremhorst, and S. Nešić, Large-eddy simulation of heat transfer downstream of a backward-facing step, J. Turbul. **5**, N20 (2004).
[30] K. Akselvoll and P. Moin, Large eddy simulation of turbulent confined coannular jets and turbulent flow over a backward facing step, Ph.D. thesis, Stanford Univ., Department of Mechanical Engineering, 1995.
[31] A. Passalacqua, Implementation of the dynamic Smagorinsky SGS model as proposed by Lilly (1992) for OpenFOAM, Git Repository, 2010, https://github.com/AlbertoPa/dynamicSmagorinsky.